Microscopy with microlens arrays: high throughput, high resolution and light-field imaging

Antony Orth[1,*] and Kenneth Crozier[1,2]

[1]*School of Engineering and Applied Sciences, Harvard University, 33 Oxford St., Cambridge, Massachusetts. 02138, USA*

[2]*kcrozier@seas.harvard.edu*

[*]*aorth@fas.harvard.edu*

Abstract: We demonstrate highly parallelized fluorescence scanning microscopy using a refractive microlens array. Fluorescent beads and rat femur tissue are imaged over a 5.5 mm x 5.5 mm field of view at a pixel throughput of up to 4 megapixels/s and a resolution of 706 nm. We also demonstrate the ability to extract different perspective views of a pile of microspheres.

OCIS codes: (170.2520) Fluorescence microscopy; (170.5810) Scanning microscopy; (350.3950) Micro-optics.

References and links

1. R. Pepperkok and J. Ellenberg, "High-throughput fluorescence microscopy for systems biology," Nat. Rev. Mol. Cell Biol. **7**(9), 690–696 (2006).
2. P. Lang, K. Yeow, A. Nichols, and A. Scheer, "Cellular imaging in drug discovery," Nat. Rev. Drug Discov. **5**(4), 343–356 (2006).
3. E. Schonbrun, A. R. Abate, P. E. Steinvurzel, D. A. Weitz, and K. B. Crozier, "High-throughput fluorescence detection using an integrated zone-plate array," Lab Chip **10**(7), 852–856 (2010).
4. E. Schonbrun, P. E. Steinvurzel, and K. B. Crozier, "A microfluidic fluorescence measurement system using an astigmatic diffractive microlens array," Opt. Express **19**(2), 1385–1394 (2011).
5. Molecular Devices ImageXpress Micro product website, *http://www.highthroughputimaging.com/screening/imagexpress_micro.html#apps*, accessed 2 April 2012.
6. S. Yazdanfar, K. B. Kenny, K. Tasimi, A. D. Corwin, E. L. Dixon, and R. J. Filkins, "Simple and robust image-based autofocusing for digital microscopy," Opt. Express **16**(12), 8670–8677 (2008).
7. R. S. Weinstein, M. R. Descour, C. Liang, G. Barker, K. M. Scott, L. Richter, E. A. Krupinski, A. K. Bhattacharyya, J. R. Davis, A. R. Graham, M. Rennels, W. C. Russum, J. F. Goodall, P. Zhou, A. G. Olszak, B. H. Williams, J. C. Wyant, and P. H. Bartels, "An array microscope for ultrarapid virtual slide processing and telepathology. Design, fabrication, and validation study," Hum. Pathol. **35**(11), 1303–1314 (2004).
8. J. Wu, X. Cui, G. Zheng, Y. M. Wang, L. M. Lee, and C. Yang, "Wide field-of-view microscope based on holographic focus grid illumination," Opt. Lett. **35**(13), 2188–2190 (2010).
9. J. Wu, G. Zheng, Z. Li, and C. Yang, "Focal plane tuning in wide-field-of-view microscope with Talbot pattern illumination," Opt. Lett. **36**(12), 2179–2181 (2011).
10. A. Tripathi and N. Chronis, "A doublet microlens array for imaging micron-sized objects," J. Micromech. Microeng. **21**(10), 105024 (2011).
11. E. Schonbrun, S. S. Gorthi, and D. Schaak, "Microfabricated multiple field of view imaging flow cytometry," Lab Chip **12**(2), 268–273 (2011).
12. M. Levoy, Z. Zhang, and I. McDowall, "Recording and controlling the 4D light field in a microscope using microlens arrays," J. Microsc. **235**(2), 144–162 (2009).
13. E. Schonbrun, W. N. Ye, and K. B. Crozier, "Scanning microscopy using a short-focal-length fresnel zone plate," Opt. Lett. **34**(14), 2228–2230 (2009).
14. H. J. Tiziani, R. Achi, R. N. Krämer, and L. Wiegers, "Theoretical analysis of confocal microscopy with microlenses," Appl. Opt. **35**(1), 120–125 (1996).
15. P. H. Nussbaum, R. Volkel, H. P. Herzig, M. Eisner, and S. Haselbeck, "Design, fabrication and testing of microlens arrays for sensors and microsystems," Pure Appl. Opt. **6**(6), 617–636 (1997).
16. A. Schilling, R. Merz, C. Ossmann, and H. P. Herzig, "Surface profiles of reflow microlenses under the influence of surface tension and gravity," Opt. Eng. **39**(8), 2171–2176 (2000).
17. Deconvolution Lab, *http://bigwww.epfl.ch/algorithms/deconvolutionlab/*, accessed 14 December 2011.

#163723 - $15.00 USD Received 27 Feb 2012; revised 6 Apr 2012; accepted 29 Apr 2012; published 1 Jun 2012

18. F. T. O'Neill and J. T. Sheridan, "Photoresist reflow method of microlens production part II: analytic models," Optik (Stuttg.) **113**(9), 405–420 (2002).
19. T. Wilson and A. R. Carlini, "Size of the detector in confocal imaging systems," Opt. Lett. **12**(4), 227–229 (1987).
20. Y. Gao and M. L. Kilfoil, "Accurate detection and complete tracking of large populations of features in three dimensions," Opt. Express **17**(6), 4685–4704 (2009).
21. S. Preibisch, S. Saalfeld, and P. Tomancak, "Globally optimal stitching of tiled 3D microscopic image acquisitions," Bioinformatics **25**(11), 1463–1465 (2009).
22. Y. Li and J. Bechhoefer, "Feedforward control of a closed-loop piezoelectric translation stage for atomic force microscope," Rev. Sci. Instrum. **78**(1), 013702–013710 (2007).
23. E. Schonbrun, C. Rinzler, and K. B. Crozier, "Microfabricated water immersion zone plate optical tweezer," Appl. Phys. Lett. **92**(7), 071112–071115 (2008).

1. Introduction

Fluorescence microscopy techniques are a workhorse of biological research, allowing highly specific imaging of cellular machinery [1]. When performed in a high throughput manner, fluorescence microscopy generates a large amount of data characterizing a biological assay that can be used for drug discovery, for example [2–4]. For high content screening applications, widefield epifluorescent microscopy is typically used, while for higher resolution applications, Nipkow spinning disk confocal systems are employed. Large areas of a fluorescent sample are imaged by stitching together smaller fields of view (FOV). The resolution of these systems depends on the desired application, and typically falls between 500 nm and 2 μm [5]. Each FOV must be obtained sequentially, with the sample being driven by a motorized stage. Crucially, the stage must come to rest for each image acquisition to prevent motion blur and to allow for focusing, thereby limiting pixel throughput to the order of a few megapixels/second (Mpx/s) [5, 6]. Modern digital cameras, however, are easily capable of megapixel frame readout at speeds of hundreds or even thousands of frames per second (fps). This suggests that substantial improvements in imaging throughput are possible if techniques are developed for which stage movement is not a limiting factor.

A few approaches for improving imaging throughput have been explored in recent years. One implementation uses an array of compound microlenses, each one of which images a separate area of a microscope slide [7]. Another technique, holographic scanning microscopy (HSM), employs a hologram to create an array of focal spots at the sample plane [8]. The transmitted light is imaged onto a charge-coupled device (CCD) image sensor by a relay telescope. Imaging proceeds by recording the intensity of the transmitted light for each focal spot while the sample is scanned. This technique takes advantage of a high throughput camera, and the holographic approach allows for a long working distance. However, the authors observe significant stage jitter and ghosting from diffraction by high spatial frequencies, both degrading image quality [8]. The chromatic properties of the holographic focusing element can be used to scan the focus grid axially [9], but this approach would present challenges for imaging multiple fluorescent lines. None of these techniques [7–9] have been demonstrated in fluorescence.

We present a high throughput fluorescence imaging technique using an array of high numerical aperture (NA) refractive microlenses. These are employed to illuminate the sample at discrete locations over a large area. Each microlens operates as an epifluorescent point scanning objective lens. This contrasts other geometries where each microlens relays a widefield image [10, 11]. We demonstrate high quality imaging of fluorescent microspheres and of a histological slice of stained rat femur. This is performed by scanning the stage over the pitch (55 μm × 55 μm) of the microlens array. Because this is a small region, there is no need to refocus, and the image sensor can be operated at a high frame rate. Additionally, we show that the experimental geometry employed allows for recording of parallax information in a manner analogous to light field microscopy [12]. While our demonstrations are carried out with a single laser and single type of fluorophore, our approach should also permit the

#163723 - $15.00 USD Received 27 Feb 2012; revised 6 Apr 2012; accepted 29 Apr 2012; published 1 Jun 2012

imaging of multiple fluorescent lines, as the microlenses are refractive and therefore display far smaller chromatic aberrations than diffractive lenses or holograms.

2. Experimental setup and fabrication

We use a parallelized epifluorescent geometry to both illuminate and detect fluorescence from the sample. A refractive microlens array is illuminated with a collimated laser beam with a wavelength of λ = 532nm and an output power of 38 mW. This creates an array of focal spots on the sample as shown in Fig. 1a. The sample is placed one focal length from the microlens array. The microlens array consists of a grid of 100x100 plano-convex refractive lenslets, oriented with their curved surfaces facing the sample. The working distance of the array is 26 μm, with an NA of 0.41. Fluorescence excited by each microlens focal spot at the sample is collected by the same microlens, and proceeds as an approximately collimated beam to a 100 mm relay lens [13]. The relay lens projects an image of the microlens array apertures onto a charge-coupled device (CCD) digital camera (Point Grey Grasshopper or Phantom V7) at unity magnification (Fig. 1b) through a long pass filter (λ>575nm). A variable diameter iris is placed in the back focal plane of the relay lens, which is itself conjugate to the sample plane for each microlens. The iris acts as a confocal spatial filter for each microlens in the array [14].

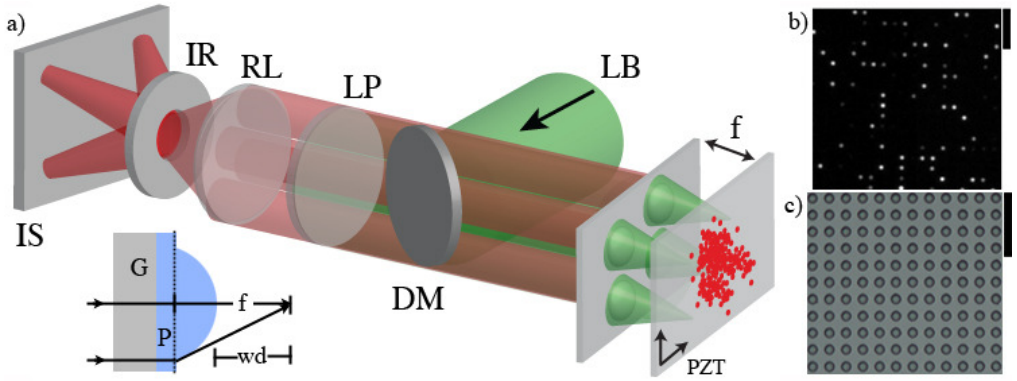

Fig. 1. (a) LB: Laser Beam; DM: Dichroic Mirror; MLA: Microlens Array; Microlens array focal length = 40.6 μm; S: Sample; PZT: Axes along which the sample is piezo scanned; LP: Long-pass Filter; RL: Relay Lens; IR: Iris; IS: Image Sensor. Inset: Schematic of a microlens, showing a central and marginal ray to define the focal length (f) and working distance (wd). G: Glass Slide; P: NOA 61 Polymer. (b) Representative raw data frame captured by the image sensor. Scale bar is 200 μm. (c) Bright-field micrograph of microlens array. Scale bar is 200 μm.

The image of the microlens array recorded on the CCD appears as an array of bright circles (Fig. 1b), with each circle representing the fluorescence relayed by a particular microlens. Each microlens acts as a point scanning confocal microscope, with its signal read out by the appropriate CCD pixels. To construct an image, the sample is raster scanned in two dimensions using a piezo stage (Thorlabs). Ideally, the scan region would be equivalent to the microlens pitch (55 μm × 55 μm). The piezo stage used, however, has a maximum travel of 20 μm × 20 μm. We therefore perform a 4x4 mosaic of scans to cover the microlens unit cell. A 4x4 mosaic, as opposed to a 3x3 mosaic, is needed provide sufficient overlap between adjacent images to allow image stitching. Because the stage must be manually adjusted between each mosaic tile, we have additional acquisition time overhead over an ideal system with a piezo stage with a long enough travel to scan over the entire microlens cell at once. This additional acquisition time overhead will be completely eliminated in future iterations by the use of a longer travel piezo stage. For this reason, we quote our acquisition times as the

#163723 - $15.00 USD Received 27 Feb 2012; revised 6 Apr 2012; accepted 29 Apr 2012; published 1 Jun 2012

elapsed time during which the piezo stage is actively scanning, and do not include the time for manual adjustment of the stage between tiles.

After scanning, images are constructed by plotting the fluorescent emission signal as a function of stage position. The fluorescent emission signal is found by summing the pixel values associated with each microlens (bright circles of Fig. 1b). For the images we present in this paper, camera frame rates of 202 or 404 frames per second (fps) are used. The number of frames acquired per line of the raster scan is 130. The line scan time is set to an integral number of camera frames to avoid image shearing.

The microlens array is fabricated via a reflow molding process [15, 16]. First, a 100x100 array of cylindrical posts is defined on a silicon wafer using AZ-40XT photoresist. The posts are 5μm tall and 40 μm in diameter. The wafer is placed on a hotplate at 125°C for 1 minute, then removed and let cool to room temperature. The heating melts the photoresist, which then takes on a smooth curved surface. After melting, each photoresist feature is 15 μm tall and 37 μm wide at its base. An inverse mold is then made from polydimethylsiloxane (PDMS) from this photoresist-on-silicon template via standard soft lithographic techniques. Finally, the photoresist template is replicated in a polymer (Norland Optical Adhesive NOA 61, n = 1.56) on a microscope slide using the inverse PDMS mold as a stamp. The resultant polymer refractive microlens array contains 10,000 elements, and is used for imaging experiments that we describe in the remainder of this paper. A micrograph of a portion of the microlens array is shown in Fig. 1c.

3. Experimental results

3.1 Microlens array characterization

We characterize the focal spots created by the microlens array by illuminating the array with a collimated laser beam (wavelength λ = 532 nm). The microlens array as fabricated on a microscope slide reflects ~6% of the incident laser illumination, attributable to Fresnel reflections at the air/glass and air/polymer interfaces. The focal spot array is imaged onto a CCD camera using a 100x 0.8NA objective lens. The focal lengths of individual microlenses, as defined in Fig. 1a are obtained as follows. The microlens array is attached to a mechanical translation stage equipped with a manually-actuated micrometer. The stage position is adjusted so that the region where the curved microlens surface becomes flat (microlens periphery) is in focus on the CCD (Fig. 1a inset). The stage position for which the microlens focal spot on the CCD camera takes maximum intensity is then found. The focal length is the distance between these stage positions. The focal length is the sum of the working distance and the lens thickness (15 μm). This process is repeated for 10 microlenses in the array. The focal lengths are measured to be 40.6 μm +/− 0.9 μm across the array; the error represents one standard deviation from the mean. The array therefore has a working distance of roughly 26 μm from the summit of the microlens to the sample. A typical focal spot created by a microlens is shown as Fig. 2. The focal spot images are deconvolved using the DeconvolutionLab plugin for ImageJ [17]. This procedure results in the full width at half maximum (FWHM) of the laser illumination focal spots being determined to be 781 nm +/− 15 nm, which is larger than the FWHM = 649 nm expected with a diffraction-limited 0.41 NA lens at 532 nm. The discrepancy is due to spherical aberration incurred reflow lens profile [18]. We perform further characterization by imaging small (200 nm diameter) fluorescent spheres. This is described in the following section.

#163723 - $15.00 USD Received 27 Feb 2012; revised 6 Apr 2012; accepted 29 Apr 2012; published 1 Jun 2012

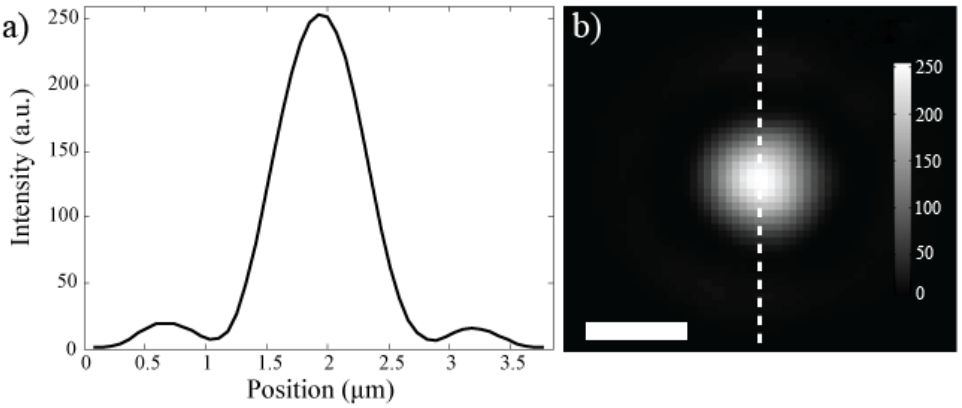

Fig. 2. (a) Line-cut of focal spot intensity. (b) Intensity distribution of a microlens focal spot. Dotted white line indicates line along which 1D intensity is plotted in panel (a). Scale bar: 1μm.

3.2 Fluorescence imaging

Samples consisting of fluorescent microspheres (Invitrogen) dried onto a microscope slide are imaged by raster scanning them under the focal spot array with a piezoelectric scanning stage. As described above, for each stage position, the CCD image sensor is read out (Fig. 1b). The signal from each microlens is integrated by summing the intensities of the pixels that comprise it. The image of the sample is then constructed by plotting the signal as a function of stage position. A typical result is shown as Fig. 3.

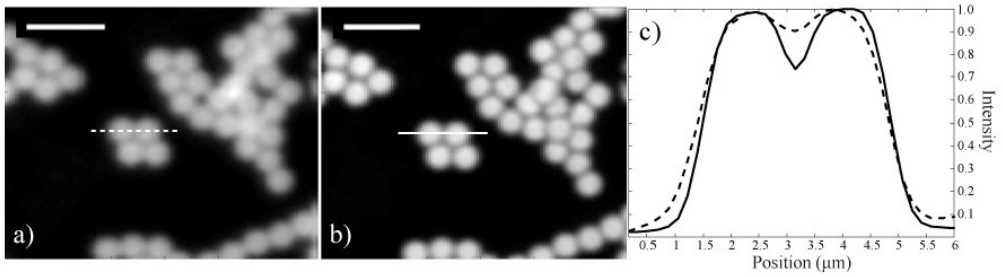

Fig. 3. (a) Image of 2 μm beads obtained with iris fully open. (b) Image of 2 μm beads with iris diameter 2 mm. Scale bar is 5 μm. (c) Line cut of intensity through a pair of neighboring beads, dotted curve: open iris, solid curve: 2mm wide iris.

The sample consists of fluorescent spheres with diameters of 2 μm. Figure 3 illustrates the effect of iris width on the image characteristics. The image taken with the iris open (Fig. 3a) is blurred compared with an image taken with a 2 mm iris width (Fig. 3b). This sharpening is evident in the line-cuts of Figs. 3a and 3b that are shown in Fig. 3c. The improved image quality is a result of confocal filtering. Overlapping images of each microlens FOV occur at the iris plane. For each microlens, the Airy disk diameter at the iris plane is $A_d = 2.44\lambda_{em}f_r/d =$ 3.8 mm, where λ_{em} is the fluorescence emission wavelength (575 nm), f_r is the focal length of the relay lens (100 mm) and d is the microlens diameter (37 μm) [14]. An iris with a diameter of 2 mm therefore functions as a confocal pinhole with a width of 0.52 of the Airy disk. To compare the results to what one would expect from the experiments of Fig. 2, we perform the following. We take the measured focal spots (Fig. 2), then construct a confocal PSF, given a 2 mm diameter iris [19]. These PSFs are convolved with two 2 μm spheres separated by a gap of 100 nm to produce the simulated image. The spheres are modeled as circles with a fluorophore density proportional to the sphere height at each point. This simulated image has

#163723 - $15.00 USD Received 27 Feb 2012; revised 6 Apr 2012; accepted 29 Apr 2012; published 1 Jun 2012

a trough to peak ratio of 0.07 +/– 0.04 for an open iris and 0.23 +/– 0.04 for a 2 mm +/– 0.25 mm diameter iris. Within experimental error, this is in agreement with the values from Fig. 3c of 0.08 and 0.27 for an open iris and 2 mm diameter iris, respectively.

The imaging of small (200 nm diameter) fluorescent beads provides an additional means for determining the system resolution. The fluorescent beads approximate a point object, effectively mapping out the PSF of the imaging system. Isolated fluorescent spheres are identified by a feature finding algorithm [20]. A 2-D Gaussian is fit to each sphere and its FWHM extracted, enabling the resolution of the system to be found. With the iris fully open (no confocal filtering), the beads have a FWHM of 787 nm +/– 39 nm, in agreement with the excitation focal spot size. With an iris diameter of 4 mm +/– 0.25 mm (~one Airy disk diameter), the FWHM of the beads drops to 706 nm +/– 34 nm. Confocal filtering of the PSF shown in Fig. 2, with an iris width of 4 mm +/– 0.25 mm, is expected to reduce the FWHM to 752 nm +/– 18 nm . The observed shrink in the FWHM of the confocal PSF agrees with theoretical expectations, within the error of our measurements.

A section of rat femur fluorescently stained with Cy3 dye is imaged using 3210 microlenses at a frame rate of 202 fps. The raw pixel throughput of the image is therefore 0.6 Mpx/s. Each frame is 304 x 304 pixels, obtained using the region of interest (ROI) function of the Phantom V7 camera employed. A 4x4 mosaic for each microlens is stitched together using a custom MATLAB script. The offsets between overlapping pairs of images are determined via 2D cross correlation, followed by gain compensation and linear blending. The FOVs from each microlens, i.e. the 4x4 mosaics, are stitched together using the same procedure with FIJI image processing software [21]. The result is shown as Fig. 4. Bone, bone marrow, fibrous structures and blood cells can all be seen in the image. The entire image takes 22 minutes of acquisition time, which does not include the time taken for manual stage adjustment between the 4x4 tiles or post processing stitching time. The manual stage adjustment overhead will be eliminated in future iterations with a longer travel piezo stage.

There are two ways in which to increase the imaging throughput of our system: using a larger number of microlenses and imaging at a greater frame rate. We achieve a raw pixel throughput of the image of 4 Mpx/s by increasing the camera frame rate to 404 fps and by using all 10,000 microlenses in the array (Fig. 5). The entire image takes 11 minutes of acquisition time, again leaving out the manual stage adjustment time and stitching time. After stitching, the image size is 0.85 Gpx. The apparent pixel throughput after stitching is less than the raw throughput because of the overlap between tiles. This reduction in apparent throughput will be avoided with a longer travel stage. This raw throughput of 4Mpx/s is nearly as high as what, at the time of writing, comprises the state-of-the-art, for example the Molecular Devices ImageXpress Micro, which achieves ~4-5Mpx/s under similar conditions and before stitching is factored in [5].

#163723 - $15.00 USD Received 27 Feb 2012; revised 6 Apr 2012; accepted 29 Apr 2012; published 1 Jun 2012

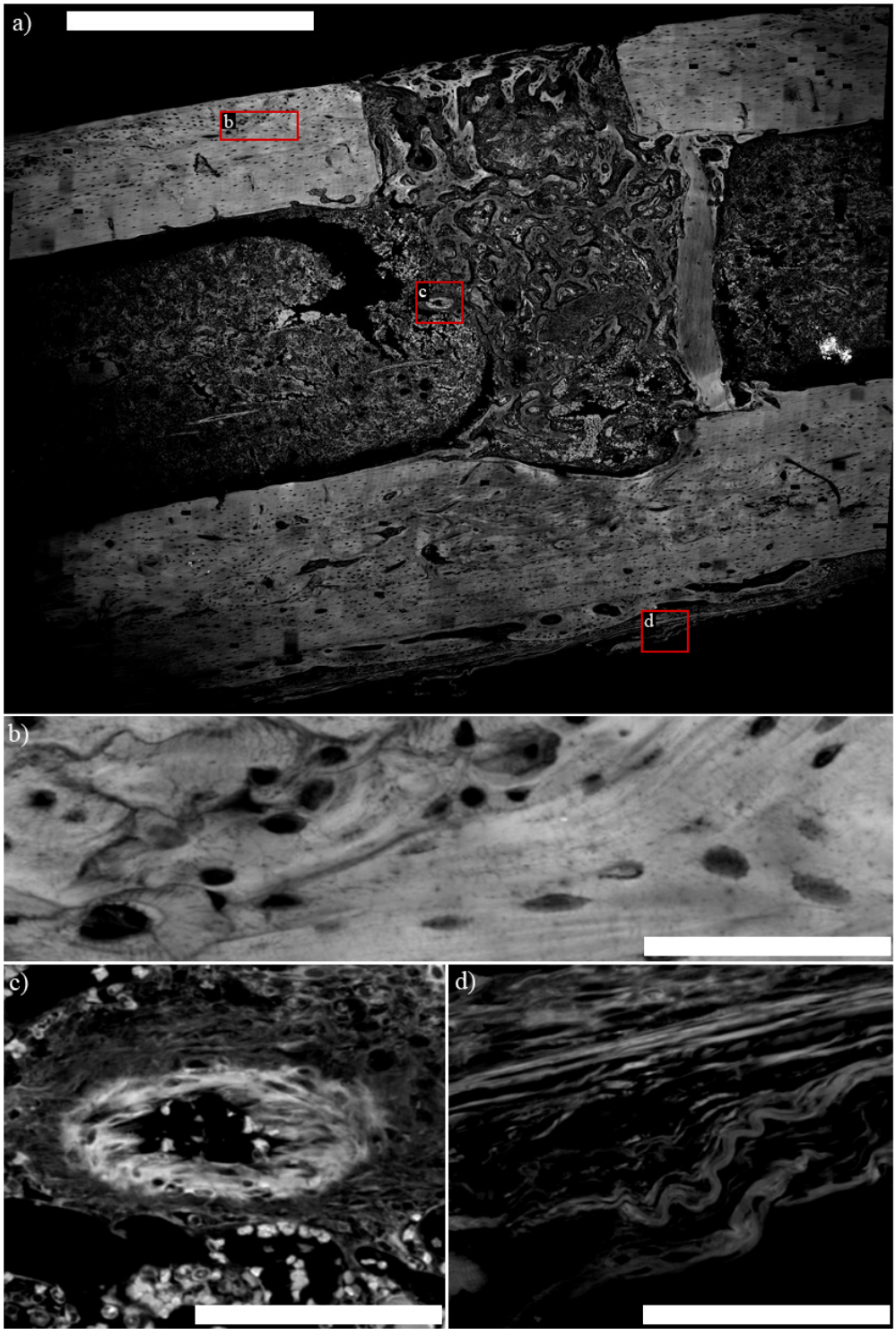

Fig. 4. (a) Image of fluorescently stained rat femur. Scale bar is 1 mm. (b) Zoom-in of cortical femoral bone. (c) Inside of the medullary canal of the femoral bone. Blood cells and fibrous structures are visible. (d) Zoom-in of periosteum. Scale bars for (b)-(d) are 80 μm.

#163723 - $15.00 USD Received 27 Feb 2012; revised 6 Apr 2012; accepted 29 Apr 2012; published 1 Jun 2012

The sample in Fig. 5 is larger than the rat femur sample, and consists of fluorescent microspheres with diameters of 2 μm. At this frame rate, the camera (Phantom V7) operates with a frame size of 352px x 352px. We therefore adjust the magnification of the relay lens system so that the image of the microlens array fits within this frame size. This corresponds to a sampling density of 12 pixels per microlens at the image sensor – a factor of 3 larger than theoretically necessary according to the Nyquist criterion. In future iterations, we expect to use the full frame of Mpx-sized camera sensors, as opposed to the 0.124 Mpx ROI used here, in order to increase the pixel throughput by over an order of magnitude.

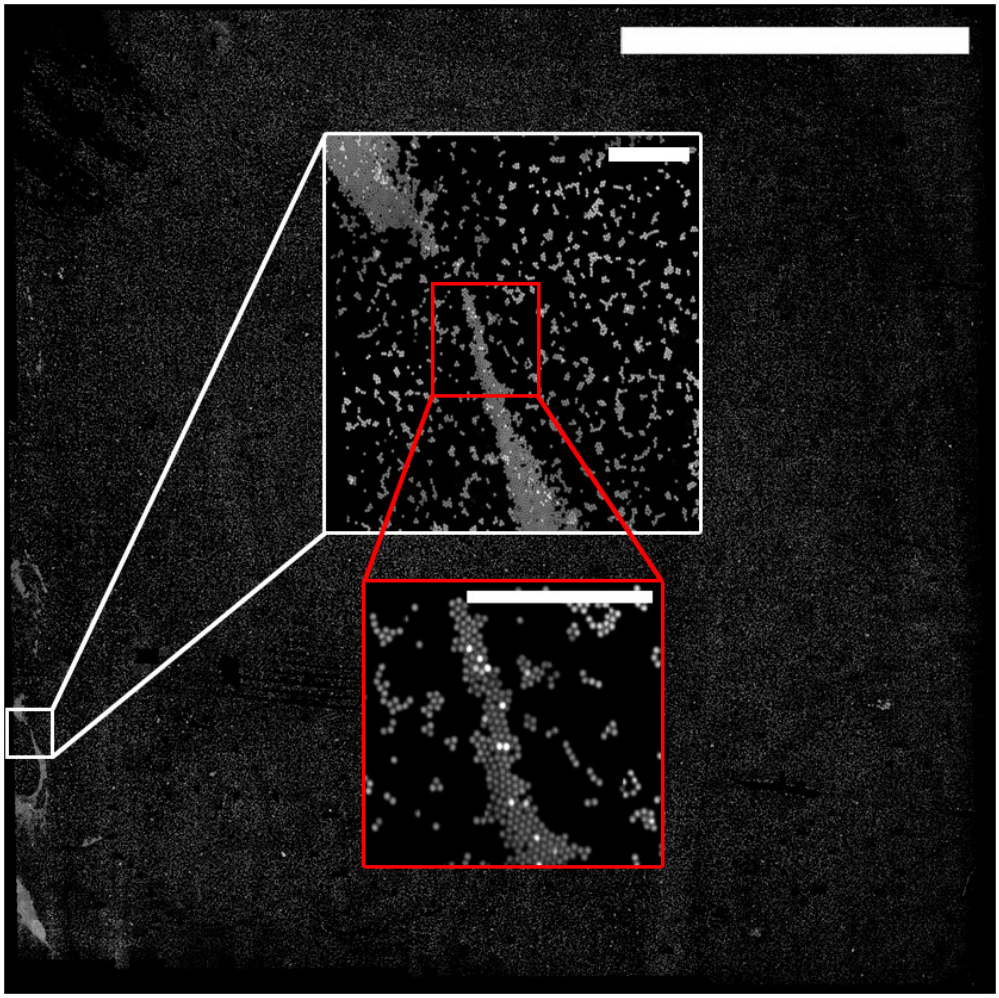

Fig. 5. A 5.5 mm x 5.5 mm image of 2μm fluorescent beads. Scale bar is 2 mm. Top inset: Zoom-in of boxed-in region (white border). Scale bar is 50μm. Bottom inset: Zoom-in of boxed-in region in top inset (red border). Scale bar is 25μm..

If the line scan frequency is increased beyond ~3Hz, mechanical resonances in the piezoelectric stage are excited and lead to artifacts in the image. This limit can be overcome by using pre-filtering approaches [22] or a piezoelectric stage with improved mechanical properties. It is the piezo line scan frequency, rather than stage velocity, that determines whether mechanical resonances are excited. Increasing the length of each scanned line, e.g. from 20 μm to 60 μm, will increase pixel throughput in a linear fashion, provided that the line

#163723 - $15.00 USD Received 27 Feb 2012; revised 6 Apr 2012; accepted 29 Apr 2012; published 1 Jun 2012

scan frequency is not modified. This assumes of course that the camera can accommodate the increased pixel throughput.

3.3 Light field imaging

A ray optics picture of the experimental setup is depicted in Figs. 6a and 6b. Because imaging is performed by a point scanning procedure, all rays emanate from a pseudo point source on the sample. Therefore, the position at which a ray hits the microlens aperture corresponds directly to the direction in which the ray emanated from the sample. Knowledge of both the initial position *(u,v)* of the ray in the sample plane and its position of intersection with another plane *(s,t)* parallel to the sample plane, fully parametrizes the ray. The 4-D data set composed of the intensity at each *(u,v,s,t)* coordinate is called the "light field function" and is denoted by *L(u,v,s,t)*. Light field recording has been previously used in microscopy to obtain perspective views and to perform refocusing [12].

The experimental geometry employed in this work images the irradiance at the microlens aperture. The scan position corresponds to the *(u,v)* position while the pixel position in the microlens subimage gives the *(s,t)* coordinate. As a result, the light field function *L* is obtained in addition to the conventional image. The conventional images (such as those shown in Figs. 3-5) are obtained by integrating the irradiance over the entire microlens aperture. This can equally be thought of as an integral over all ray angles impinging on the microlens.

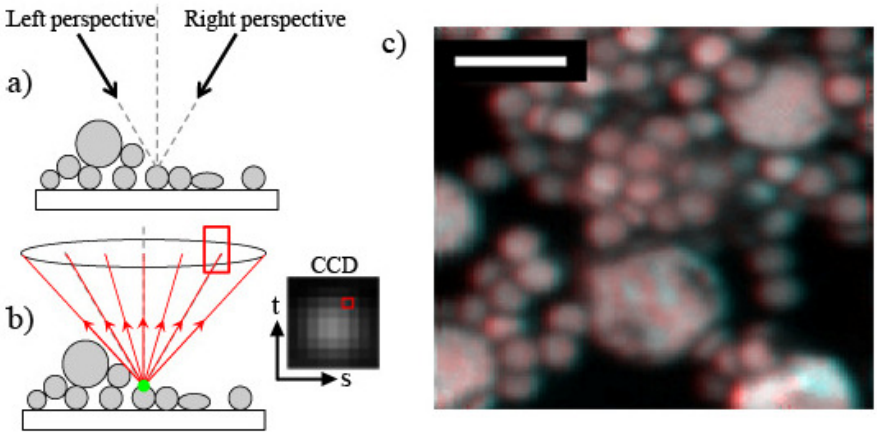

Fig. 6. (a) Left and right perspective views are observations of a scene taken from opposing viewpoints. b) Ray-optics schematic of angular mapping onto image sensor. The angular distribution of rays emitted from within the excitation spot (green region) corresponds to the intensity distribution impinging on the lens aperture and its image at the image sensor. Each pixel on the CCD image of the microlens aperture corresponds to a distinct perspective view. The space occupied by the image of the microlens aperture is described by the coordinates *(s,t)*. (c) Red/cyan anaglyph of a pile of 2μm and 5μm fluorescent beads, constructed using left and right perspective images (Media 1 shows this sample from multiple perspectives). Scale bar is 5μm.

We can digitally filter the irradiance to acquire light field images at specific $(s = s_0, t = t_0)$ planes. This is done by using only the (s_0,t_0) pixel in a microlens subimage to construct the raster scanned image, effectively replacing the detection optics by a pinhole at position (s_0,t_0). Each *(s,t)* coordinate corresponds to a unique viewpoint. As the viewpoint is changed, beads that are out of the focal plane appear to shift position; this is the basis of depth perception. Figure 6c shows an anaglyph of a pile of beads, constructed by overlaying images obtained from two diametrically opposed pixels in the microlens aperture, color coded as red and cyan. The two diametrically opposed pixels lie halfway to the edge of the microlens from its center. The angle between the red and cyan colored images is 24°. The parallax and three-

#163723 - $15.00 USD Received 27 Feb 2012; revised 6 Apr 2012; accepted 29 Apr 2012; published 1 Jun 2012

dimensional structure of the sample is particularly evident in Fig. 6c (Media 1), in which the viewpoint is made to circulate at 12° from the vertical.

The maximum angle of parallax is limited by the collection angle of the microlens. In this work, the microlens NA is 0.41 in air so that the maximum collection angle is 48.4°. The angular resolution is dependent on the iris diameter. The iris acts as a low pass filter for the microlens array image projected onto the camera sensor. As the iris is stopped down, there are fewer resolvable spots within a microlens aperture, and therefore the resolution in the *(s,t)* plane (equivalently the angular resolution) is degraded. This is analogous to the tradeoff described in [12], where the number of diffraction limited spots impinging on each microlens determines the angular resolution. Here, the number of diffraction limited spots sampled by each microlens is controlled by the iris in the sample's conjugate plane, i.e. the iris effectively controls the field of view of each microlens. Even though only one diffraction limited spot is illuminated in the microlens FOV, the entire spatial bandwidth relayed by the microlens is used for resolution in the *(s,t)* plane.

4. Conclusions

We have demonstrated point scanning microscopy with a refractive lens array. We demonstrated the imaging of fluorescent beads at a pixel throughput of 4Mpx/s, using a sensor area of only 352 px x 352 px. This throughput rivals the state-of-the-art commercial systems that exist at the time of writing, while only using a fraction of the active area of the image sensor. A histological slice of fluorescently stained rat femur was also imaged. Additionally, we have shown that the spatial distribution of intensity in the microlens aperture image corresponds to different perspective views of the sample. This was used to extract different perspective views and to construct a stereoscopic image of a pile of fluorescent beads. A number of interesting possibilities exist for extending this work. We note that the pixel throughput could be dramatically increased by using the entire image sensor. For example, an image sensor with N pixels can resolve up to N/4 microlenses at the Nyquist sampling limit. Using a 4 Mpx image sensor, for example, one could employ an array of 10^6 microlenses (as opposed to the 10^4 used here). In this case, a pixel throughput of up to ~400 Mpx/s would be possible, using the same scanning speed and frame rate employed here. A next generation implementation of the technique used here would able to image a well plate at ~100x the speed of current high throughput microscopes. This would be achieved by distributing the imaging over a larger area, thereby decreasing the demands of long range mechanical scanning and consequently taking advantage of the large pixel throughput of modern digital cameras. We lastly note that, for applications where spatial resolution is important, diffractive lenses could be employed, as these have been shown to achieve very high numerical apertures (e.g. 1.31 in [23]).

Acknowledgments

This work was supported by the Advanced Energy Consortium via the Bureau of Economic Geology at the University of Texas at Austin. The authors thank Dr Manav Mehta and Professor David Mooney of the Harvard School of Engineering and Applied Sciences for providing the rat femur sample. Fabrication work was carried out at the Harvard Center for Nanoscale Systems, which is supported by the National Science Foundation.

#163723 - $15.00 USD Received 27 Feb 2012; revised 6 Apr 2012; accepted 29 Apr 2012; published 1 Jun 2012